An analysis of the observed low-level structure of rapidly intensifying and mature Hurricane Earl (2010)

Michael T. Montgomery[a*], Jun A. Zhang[b], and Roger K. Smith[c]
[a] *Dept. of Meteorology, Naval Postgraduate School, Monterey, CA, USA*
[b] *NOAA Hurricane Research Division, Miami, FL, USA*
[c] *Meteorological Institute, University of Munich, Munich, Germany*
[*]Correspondence to: Prof. Michael T. Montgomery, Dept. of Meteorology, Naval Postgraduate School, Monterey, CA 93943, USA. E-mail: mtmontgo@nps.edu

We examine dynamic and thermodynamic aspects of Atlantic Hurricane Earl (2010) during its intensification and mature phases over four days of intensive measurements. During this period, Earl underwent an episode of rapid intensification, maturity, secondary eyewall replacement, re-intensification and the early part of the decline. The observations are used to appraise elements of a new model for tropical-cyclone intensification.

The results affirm the conventional (vortex interior) and boundary layer spin up mechanisms that form dynamical elements of the azimuthally-averaged view of the new intensification model. The average maximum tangential winds beneath the eyewall are found to exceed the gradient wind by between 20% and 60%. The results suggest also that the gradient wind balance approximation in the low-level vortex interior above the boundary layer may not be as accurate as has been widely held in the inner-core region of a tropical cyclone during its intensification. An analysis of the low-level thermodynamic structure affirms the radial increase of moist equivalent potential temperature, θ_e, with decreasing radius during the intensification process, a necessary ingredient of the new model for maintaining convective instability in the presence of a warming upper-troposphere. An unanticipated finding is the discovery of an unmixed boundary layer in terms of θ_e over several hundred kilometers of the vortex. In the inner-core region, this finding is not consistent with the axisymmetric eruption of the boundary layer into the eyewall unless there are non-conservative (eddy) processes acting to modify the entropy of ascending air.

Key Words: Hurricanes, typhoons, conventional spin-up mechanism, boundary layer spin-up mechanism, thermodynamic structure, surface enthalpy fluxes, GRIP

Received February 27, 2013; Revised October 22, 2013; Accepted

Citation: ...

1. Introduction

Early theories of tropical-cyclone intensification emphasized the role of deep convective clouds, which, in an azimuthally-averaged sense, generate radial convergence in the low to mid-troposphere (Charney and Eliassen 1964, Ooyama 1964). These authors showed that spin up was a result of the accompanying import of absolute angular momentum, M, above the frictional boundary layer, where M is materially conserved. Here $M = rv + 1/2fr^2$, where

r denotes radius from storm centre, v denotes azimuthally-averaged, storm-relative tangential velocity and f denotes the Coriolis parameter.

Dissatisfied by thermodynamical aspects of the foregoing studies, Ooyama formulated a highly simplified three-layer slab model with an entraining-plume representation of deep convection on the vortex scale and of sensible and latent heat fluxes from the underlying ocean (Ooyama 1969). As in the earlier models, the spin up was associated with the convectively-induced import of M, but that spin up required a supply of latent heat energy from the ocean to maintain the (parameterized) deep convection. We will refer to the convectively-induced import of M above the boundary layer, in conjunction with the supply of moisture from the underlying ocean surface, as the conventional intensification model (Ooyama 1969, 1982, Willoughby 1988, 1995).

A seemingly different model for spin up was proposed by Emanuel (1997) that focussed more on the thermodynamic controls on the intensification process, but as noted by Montgomery and Smith (2013), the dynamical mechanism for spin up appears to be again the radial import of M above the frictional boundary layer by deep convection. An appraisal of these early paradigms for tropical-cyclone intensification, all of which are axisymmetric is given by Montgomery and Smith *op. cit.*

A new paradigm for tropical-cyclone intensification has been expounded in a series of recent papers (Nguyen *et al.* 2008, Montgomery *et al.* 2009, Smith *et al.* 2009, Bui *et al.* 2009) and summarized by Montgomery and Smith (2013). This paradigm was distilled from the results of the foregoing studies using observations and high-resolution, three-dimensional, numerical model simulations that represent deep convection explicitly and recognizes the role of rotating deep convection in the spin-up process. Analyses of azimuthally-averaged fields in the foregoing simulations lead to a revised view of spin up that includes the conventional intensification mechanism, but emphasizes the important *dynamical role* of the boundary layer[1]. In fact, Smith *et al.* (2009) showed that the spin up of the maximum tangential winds takes place *within* the frictional boundary layer, although the spin up of the winds above the boundary layer (that are widely held to be in approximate gradient wind balance) is necessary as well. (A similar result was noted by Zhang *et al.* (2001) in a simulation of Hurricane Andrew (1992), but they did not appear to recognize the generality of their result.) As in the earlier paradigms, the spin up of the bulk vortex above the boundary layer occurs through the conventional mechanism as discussed above.

The boundary-layer spin up mechanism may seem counter-intuitive to those who have studied boundary layers only in the context of nonrotating flows, where friction reduces the flow near the boundary. The mechanism is possible because the inward displacement of air parcels is much larger in the boundary layer than above, a consequence of the frictional disruption of gradient wind balance that holds approximately above the boundary layer. This disruption leads to a net inward force in the boundary layer. Since the azimuthal mean tangential wind speed $v = M/r - \frac{1}{2}fr$, the possibility arises that the loss of M to the surface following an air parcel may be more than offset by a large inward displacement of the air parcel so that the tangential wind increases and eventually becomes larger than that above the boundary layer. In high resolution model simulations, the process is exemplified by time-height cross-sections of the azimuthally-averaged M-surfaces, which tilt inwards with height within the boundary layer and outwards with height above with a "nose" at the top of the boundary layer. While there have been observations of such nose-like structures in a mature hurricane (e.g. Bell and Montgomery 2008), to our knowledge the evolution of the M-surfaces during intensification has not been reported for an intensifying tropical cyclone.

While the boundary layer spin up mechanism presumes an increasing gradient wind and radial pressure gradient at the top of the boundary layer in association with the conventional mechanism, it contributes also to the spin up of the bulk vortex through the lofting of the enhanced tangential momentum into the bulk vortex and a corresponding adjustment of the bulk wind and mass fields toward the higher winds from the boundary layer.

In a nutshell, on the system-scale, the new spin up paradigm has two dynamical components. The first is the conventional spin up mechanism, i.e., convectively-induced inflowing rings of air in the lower troposphere that approximately materially conserve their M. The second component comprises the boundary-layer spin-up mechanism summarized in the foregoing discussion. A related and essential ingredient of the new spin up paradigm is the maintenance of convective instability in the inner-core region of the vortex as discussed above.

Although the focus of the present study is on the low-level structure of both the intensification and mature phases of a hurricane, some aspects of Emanuel's steady-state hurricane model (Emanuel 1986, henceforth E86) still provide a useful context for interpreting observations of an intensifying storm. An important feature of this model is the assumption that as air parcels ascend along the eyewall, they conserve their absolute angular momentum, M, and saturation pseudo-equivalent potential temperature, θ_e^*, so that M and θ_e^* surfaces are congruent. In addition, the theory assumes explicitly that the tangential flow above the boundary layer is in gradient wind balance. An important constraint in the model is the rate at which M and θ_e^* vary with radius in the boundary layer inside the radius of maximum tangential wind speed (r_m), which E86 assumes to be located at the outer edge of the eyewall (see E86, Figure 1). A brief summary of the model formulation is contained in section 2 of Smith *et al.* (2008). While the model has undergone a number of reincarnations over the years (Emanuel 1988, Emanuel 1995, Bister and Emanuel 1998, 2002, Emanuel 2004, Emanuel and Rotunno 2011, Emanuel 2012), the foregoing aspects have remained unchanged.

An important feature of the E86 model is the increase in θ_e^* with diminishing radius in the vicinity of the

[1]In this work we adopt a dynamical definition of the boundary layer, using the term boundary layer to describe the shallow layer of strong inflow near the sea surface that is typically 500m to 1 km deep and which arises largely because of the frictional disruption of gradient wind balance near the surface (e.g., Figure 6 of Smith *et al.* 2009). This dynamical definition is uncontroversial in the outer regions of a tropical cyclone vortex, where there is subsidence into the boundary layer, but it has limitations in the inner-core region where boundary-layer air is being lofted into the eyewall clouds. In the latter region, conventional boundary-layer theory breaks down. For one thing, vertical perturbation pressure gradients may not be ignored there. The flow in this region is akin to that of separation in aerodynamic boundary layers. For further discussion on hurricane boundary layers see Smith and Montgomery (2010). Here, we acknowledge this limitation, but adopt the layer of relatively strong inflow as the boundary layer.

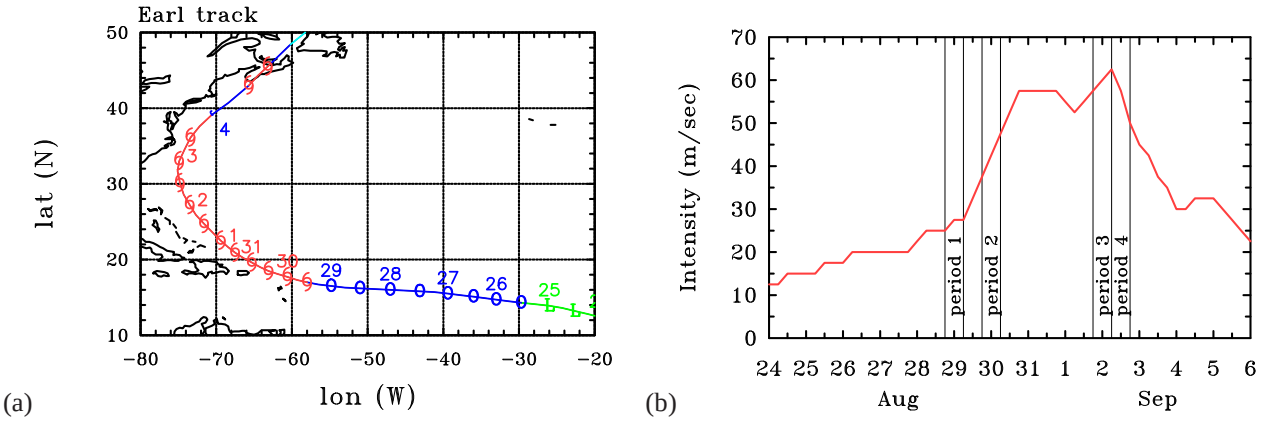

Figure 1. (a) Best track positions, and (b) intensity for Hurricane Earl, 25 August - 4 September 2010. Based on "best track" data from the National Hurricane Center archive. Vertical lines in (b) delineate four periods of flight reconnaissance referred to in the text.

eyewall updraught. Such a feature had been documented earlier from observational analyses (Hawkins and Imbembo 1976) and has been confirmed by more recent work (Montgomery *et al.* 2006, Marks *et al.* 2008, Bell and Montgomery 2008). Since the virtual temperature, θ_v, in cloud increases monotonically with θ_e^*, θ_v must increase also with decreasing radius at a given pressure level, consistent with the warm core structure of the vortex. Because ascending air parcels move to larger radii, the M and θ_e^* surfaces flare outwards with height. As these air parcels move outwards conserving M they spin more slowly about the rotation axis of the storm. This fact, together with the positive radial gradient of M, explains the observed decrease of the tangential wind speed with height, consistent with the thermal wind equation (E86). As discussed by Montgomery and Smith (2013), in the new intensification paradigm, only modest surface moisture fluxes are required from the underlying ocean, which give rise to an increase of boundary layer θ_e with decreasing radius. The θ_e increase is needed to help maintain a degree of convective instability of the inner-core region in the presence of a developing warm core aloft. This increase does not necessarily require an evaporative-wind feedback process as hypothesized by Emanuel *et al.* (1994) and Emanuel (2003). In fact, Montgomery *et al.* (2009) have shown that this evaporative-wind feedback mechanism is neither essential nor the dominant pathway for tropical cyclone spin up.

Observational support of the second spin-up mechanism for tropical cyclone intensification was presented by Sanger (2011) and Sanger *et al.* (2013) who examined the azimuthally-averaged boundary layer structure during the intensification of typhoon Jangmi, which was observed as part of the Tropical-Cyclone -Structure 2008 (TCS08) experiment (Elsberry and Harr 2008). An even more detailed data set for testing this spin-up mechanism and the new intensification paradigm was obtained in Hurricane Earl (2010) during four days of intensive measurements based on airborne dropwindsondes released from the upper troposphere during the collaborative National Aeronautics and Space Administration (NASA), Genesis and Rapid Intensification Processes (GRIP) and the National Oceanic and Atmospheric Administration (NOAA), Intensity and Foreasting Experiment (IFEX). Here we examine the kinematic, dynamic and thermodynamic and thermodynamic structure of this Atlantic hurricane during its intensification and mature phases. During the extensive observation period, Earl underwent one episode of rapid intensification and the measurements afford a unique opportunity to assess several aspects of the new paradigm of tropical cyclone intensification. They afford also the possibility of extending the analysis of Smith and Montgomery (2013a) to quantify the changes in the radial distribution of boundary-layer θ_e as the storm intensifies. Like the study by Sanger *et al.* (2013), we will adopt a system-scale viewpoint of the intensification process and use a composite methodology to construct an approximate azimuthally-averaged picture of the evolving vortex. An analysis of the asymmetric processes is beyond the scope of this study.

The paper is organized as follows. In section 2 we give a brief summary of Hurricane Earl, focussing largely on the period from rapid intensification to maturity. In section 3 we summarize the data quality and analysis methodology employed. Sections 4 and 5 present the analysis of the observational data. Section 6 presents a summary of the main findings and discusses some implications of the results.

2. Hurricane Earl and data collected

Hurricane Earl originated from a strong tropical wave that left the west coast of Africa on 23 August. The U.S. National Hurricane Center (NHC) "best track" chart of Earl's path is given in Figure 1a, with the time series of its intensity shown in Figure 1b. The following description is based on the storm summary produced by the NHC.

Strong subtropical ridging over the eastern Atlantic steered Earl westwards to west-north-westwards at a speed of between 7.5 and 10 m s^{-1} for the next few days. At the same time, the tropical storm strengthened gradually over a sea surface temperature of 28-29C and in an environment of light to moderate vertical shear. Data from an Air Force Reserve reconnaissance aircraft indicate that Earl became a hurricane by 1200 UTC [2] 29 August, when centred about 220 n mi east of the northern Leeward Islands. Around that time, Earl neared a weakness in the subtropical ridge associated with Hurricane Danielle to its west, and it slowed and gradually turned northwestward while undergoing rapid intensification. Earl strengthened to a Category 3 hurricane about 12 h later when it was located very near the northern Leeward Islands. Data from both NOAA and Air Force

[2]Universal Time Coordinated

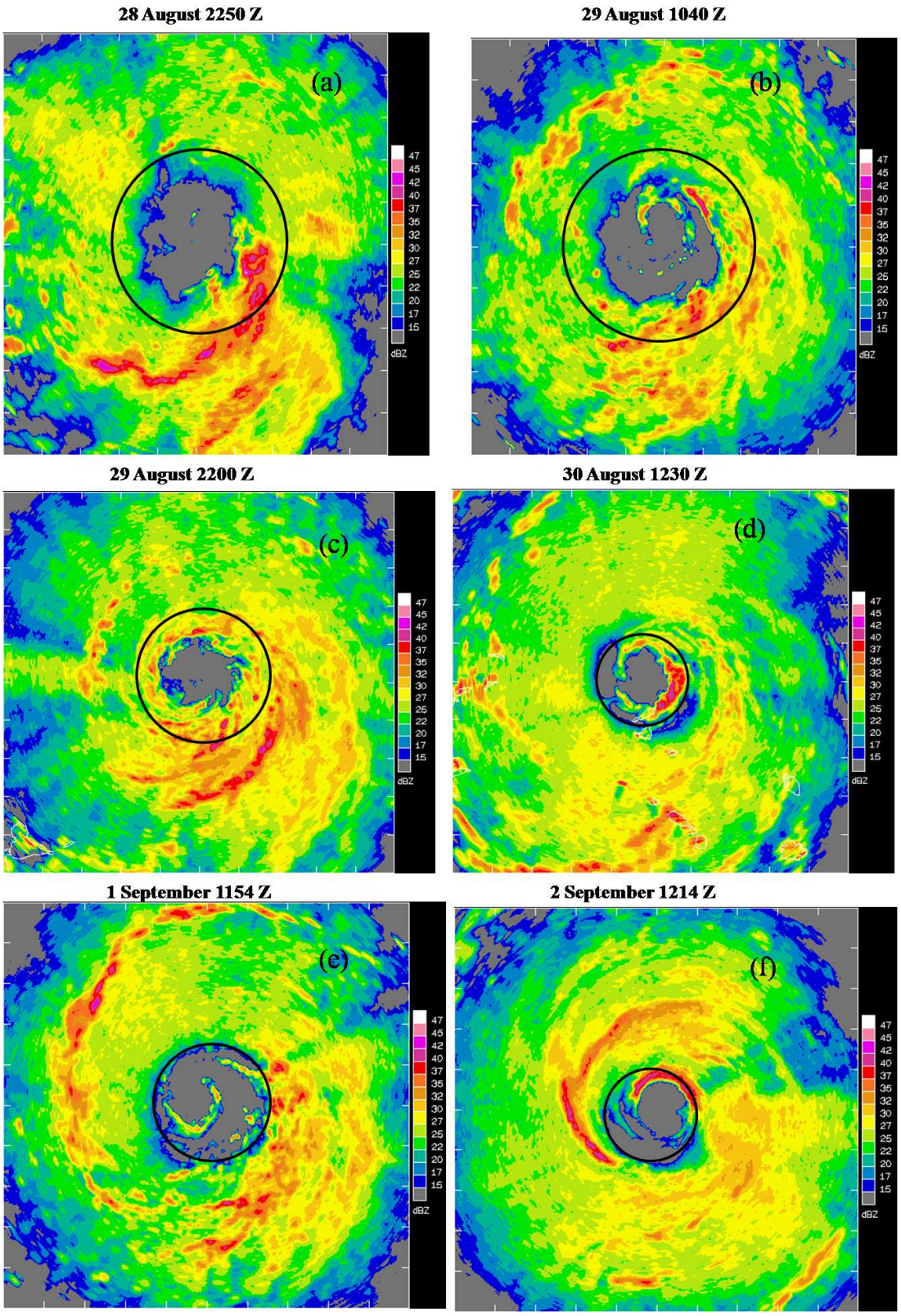

Figure 2. The reflectivity field as viewed by the lower fuselage radar of the NOAA WP-3D aircraft at (a) 2250 UTC 28 August, (b) 1040 UTC 29 August, (c) 2200 UTC 29 August, and (d) 1230 UTC 30 August. All four panels are 360 km x 360 km. The colour bar shows values in ranges of dBZ. The bold circles denote the radius of maximum azimuthally-averaged, storm-relative tangential wind deduced from the Doppler radar data.

hurricane hunter aircraft, along with satellite imagery, indicate that Earl intensified by 40-kt over 24 h, becoming a Category 4 hurricane by 1800 UTC 30 August.

Figure 2 shows a composite reflectivity from the lower-fuselage (5 cm) radar on the NOAA P3 aircraft during four missions into the intensifying storm. The reflectivity image centred at 2250 UTC 28 August shows a cyclonically curved band of high reflectivity (exceeding 40 dBZ) that extends from the southwest to the east of the centre. At this time the developing eye, which is marked in the centre

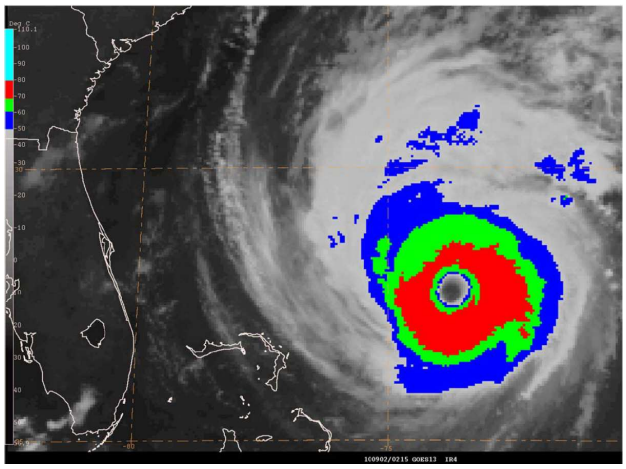

Figure 3. An infrared satellite image at 0215 UTC 2 August 2010 of Hurricane Earl near its peak intensity.

by very low reflectivity values (below 15 dBZ), has an approximately oval shape with diameter of 60 km in the east-west direction and 80 km in the north-south direction. By 1040 UTC 29 August the eye boundary has become more circular and the reflectivity pattern become a little more symmetric about the centre. During the next 12 hours the eye region has contracted and remains approximately symmetric with a final diameter of approximately 50 km. at 2200 UTC 29 August. Again, the reflectivity pattern has become asymmetric with two prominent reflectivity bands wrapping cycloncally inwards on the southeastern side of the centre. It is during this interval that the vortex intensifies rapidly (cf. Figure 1b). After another 12 hours by 1230 UTC 30 August the eye has contracted further and is almost surrounded by a narrow region of high reflectivity, characterizing a developing eyewall. The reflectivity of this eyewall is most extensive in the southeast sector. The bands of high reflectivity in the previous image have disappeared. A moat of low reflectivity is apparent mainly on the western and southwestern sides of the eye. The intensity at this time is approximately 55 m s^{-1}.

Subsequently, Earl began a concentric eyewall replacement cycle that was well observed in both the San Juan Doppler radar and aircraft flight level wind data. This cycle halted the intensification process and Earl remained a 115-kt hurricane for the next 24 h. Southwesterly shear increased late on 31 August, which resulted in Earl weakening back to a Category 3 hurricane by 0000 UTC 1 September. Earl weakened a little more during the morning hours of 1 September, but by that afternoon the eye became more distinct and deep convective activity increased and gained symmetry, presumably due to a decrease in vertical shear. Earl re-intensified to Category 4 strength by 1800 UTC 1 September and reached its peak intensity of 63 m s^{-1} 12 h later, when it was located about 380 n mi southeast of Wilmington, North Carolina. An infrared satellite image of Earl near its peak intensity is shown in Figure 3. Earl then rapidly weakened as it turned northwards, falling below major hurricane status by 0000 UTC 3 September.

3. Data quality and analysis methodology

Hurricane Earl was extensively sampled by multiple research and reconnaissance aircraft from NOAA, NASA and the United States Air Force prior to, during, and at the end of the period of rapid intensification, with less than 12 h between sampling times for the inner core and less than 24 h for the environment. This represents one of most intensively-sampled lifecycles of rapid intensification ever. In our analyses, we use the Global Positioning System (GPS) dropwindsonde (henceforth dropsonde) data collected in Hurricane Earl between 28 August and 2 September, 2010. As an example, Figure 4 shows the dropsonde data coverage relative to the storm centre obtained from four different research aircraft. The position of each dropsonde shown corresponds to the position when the dropsonde was first released, but analyses in the forthcoming section use the instantaneous position of the dropsonde at a particular height. We group the data into 12 hour windows to increase the sample size and focus on four periods, two during the period of rapid intensification (18 UTC 28 August to 6 UTC 29 August (period 1); and 18 UTC 29 August to 6 UTC 30 August (period 2) and two in which Earl had reached a quasi-steady state (18 UTC 1 September to 6 UTC 2 September (period 3); and 6 UTC 2 September to 18 UTC 2 September (period 4)). These four periods are indicated in Figure 1b. Table 1 presents an overall summary of the dropsonde analysis periods, eyewall composite region, number of dropsondes used to form the composite, and the total number dropsondes within 250 km radius.

All the dropsonde data were quality controlled using the ASPEN software, which is based on the EDITSONDE software developed by the Hurricane Research Division (Franklin et al. 2003). A standard 10 s filter is used to smooth turbulent noise and switching between GPS satellites, as in Powell (2003). A more detailed description of the observational instruments inside the dropwindsonde can be found in Hock and Franklin (1999). The accuracy of the horizontal wind speed measurements is 2.0 m s^{-1} and < 0.5 m s^{-1} for the vertical winds with approximately 0.2 m s^{-1} precision. The storm centre is determined using the flight-level data using the Willoughby and Chelmow (1982) method along with the best track data record.

The radial and tangential components are computed relative to the instantaneous storm centre. We averaged the data located within the eyewall region, and found the height of the maximum mean tangential wind speed. To calculate the gradient wind at this height, first we fit the pressure data with a quadratic polynomial in a least squares sense as a function of radius from the storm centre. Next, we calculate the gradient wind by solving the quadratic gradient wind equation for tangential velocity using the inferred radial pressure gradient force (Eq. (1) below). Then, using this methodology, the radial profile of the mean gradient wind can then be compared with the local tangential wind speed at the same level (see e.g., Figure 11 later).

4. Doppler-radar analysis and results thereof

4.1. The radar data

The tail Doppler radar data from NOAAs WP-3D aircraft are used to construct storm-centred r-z plots of M for each flight. Such plots are then used to assess the first component of the new intensification paradigm of Montgomery and Smith (2013), in which the conventional intensification mechanism for the system-scale circulation discussed in the Introduction is an important element. Table 2 presents

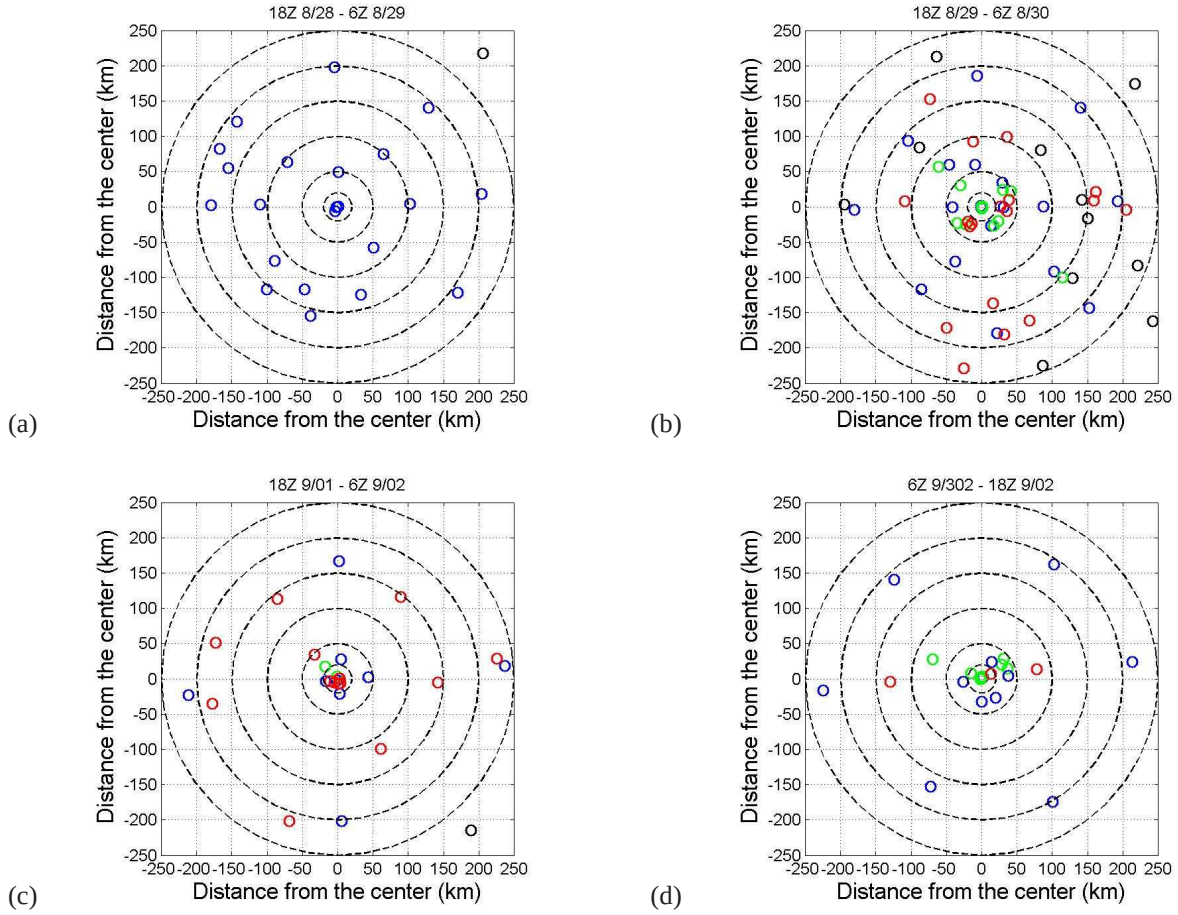

Figure 4. Storm-centred dropsonde distribution on the five days of monitoring of Earl by four different research aircraft. Each color represents one type of aircraft where dropsondes were released. Blue color represents WP-3D aircraft, red color represents DC-8 aircraft, green color represents C-130 aircraft, black color represent G-IV aircraft. For simplicity, the storm-relative horizontal trajectory of each dropsonde after release time is not shown.

Periods	Start time	End time	Eyewall range (km)	Number of sondes in the eyewall region	Total number of sondes within 250 km
1	08/28 - 18Z	08/29 06Z	95-105	3	20
2	08/29 - 18Z	08/30 06Z	35-45	4	32
3	09/01 - 18Z	09/02 06Z	20-30	3	16
4	09/02 - 06Z	09/02 18Z	25-35	3	18

Table I. Periods of interest for sonde analyses. See text for details.

Flight ID	Start time (radar)	End time (radar)	RMW (km)	Maximum M at RMW	Maximum Vt at RMW
100828I1	2132	2531	65	1.66×10^6	23.8
100829H1	0922	1318	101	2.82×10^6	25.6
100829I1	2057	2438	49	1.80×10^6	34.9
100830H1	1110	1341	35	0.82×10^6	36.2
100901H1	1056	1217	45	2.46×10^6	52.1
100902H1	0935	1213	31	1.70×10^6	55.6

Table II. Summary of P3 radar data corresponding to Figs. 2, 5 and 6. The units of M and V_t are $m^2 s^{-1}$ and ms^{-1}, respectively. See text for further details.

a summary of the radar data collected, including specific flight identification (ID), radar-derived radius of maximum tangential wind (RMW), M and V_t at the RMW.

The data are processed as follows. An automated quality control process is applied before the data analysis (Gamache 2012). The fore/aft scanning technique is used to create dual-Doppler measurements from a single radial penetration (e.g., Reasor *et al.* 2009). The Doppler radar projection equations and anelastic mass continuity equation are solved at the same time to derive the three-dimensional wind field via least-squares minimization (Gamache 1997). The quality-controlled Doppler radials extend from the surface

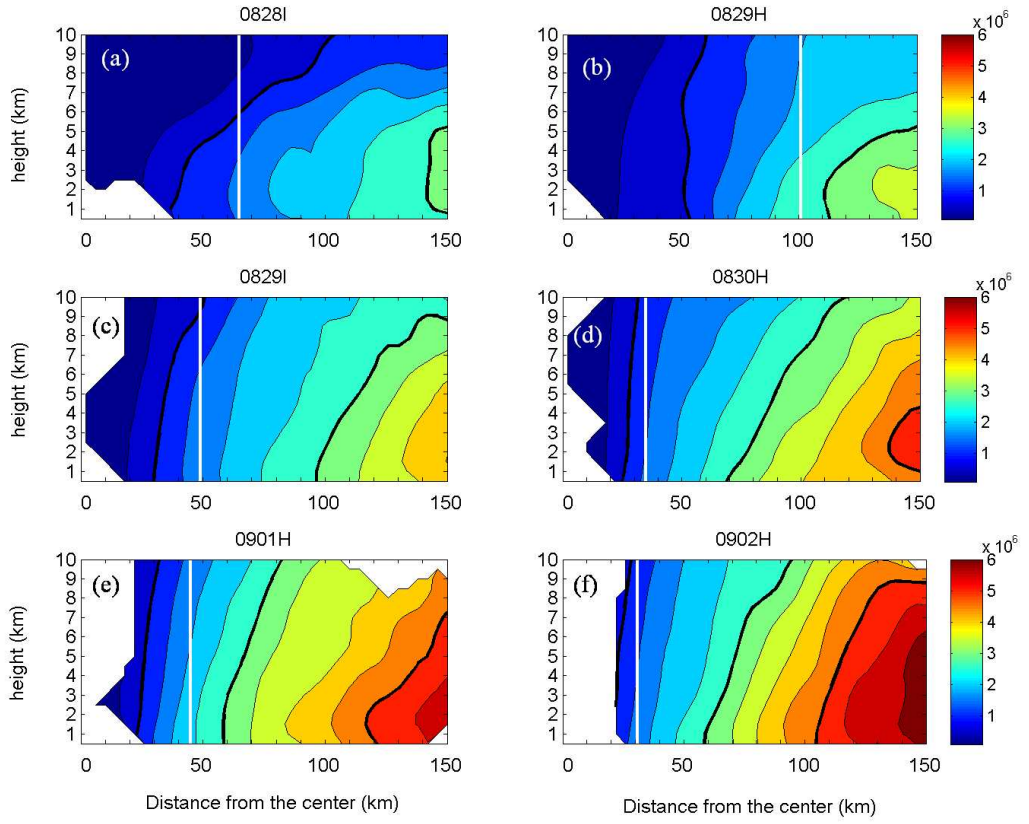

Figure 5. Evolution of absolute angular momentum, M, which is azimuthally-averaged about the storm centre. These M-data are from Doppler radar and dropwindsondes as discussed in section 4. The panels show only the deep tropospheric data above 500 m altitude. The radius of maximum azimuthally-averaged tangential velocity at 2 km altitude is indicated by the white vertical line in each panel. The time for each analysis period is detailed in Table II.

to 20 km with horizontal and vertical grid spacings of 2 km and 0.5 km, respectively. For technical reasons, the vortex centre for the radar analysis is defined using a modified version of the centre-finding method of Marks *et al.* (1992) as detailed by Reasor and Eastin (2012). This centre is very close (within a few km) to the centre determined by the Willoughby Chelmow (1982) method mentioned above and used for the dropwindsonde analysis in the next section.

To determine the distribution of azimuthally-averaged M, analyses from individual radial penetrations during each flight are merged. The purpose for merging radar swaths is to create the most complete azimuthal coverage of the core region out to the largest radii. A detailed description of the methodology used for merging the swaths and its limitations are given by Reasor *et al.* (2013). The radar data are observed mainly above 500 m, so that most of the data are above the boundary layer.

4.2. Spin up above the boundary layer

Figure 5 shows the evolution of M surfaces as calculated from the merged Doppler radar data for each flight. Note that, in calculating M, we use a constant f for each flight. The value of f is calculated using the averaged latitude of the moving storm centre for each flight. As the storms move during the period of eyewall penetrations, we have assumed that structural features of interest are quasi-steady over the observation period. Because the latitude change in the storm centre is small (< 0.6 deg) during the period of eyewall penetrations for each flight, the change in f associated with the moving storm is small ($< 3\%$), implying a negligible change of the M fields over the Doppler radar domain shown. It is evident from the figure that M increases with radius at each level during the Earl's intensification, implying that the vortex is centrifugally (or inertially) stable (e.g., Shapiro and Montgomery 1993, Franklin *et al.* 1993) and that the mean radial inflow can carry air with high M towards the centre to spin up the tangential wind field there. We see also that, indeed, over the period of observations, the M surfaces do move radially inwards. Moreover, the signature of the strengthening boundary layer inflow is evident by the increase in the upward-outward tilt of the M surfaces in the lower troposphere as these surfaces move inwards. The solid black curves are chosen to highlight a few M surfaces during the rapid intensification phase of the vortex. As an example, in the top-left panel of curve in Figure 5 (0828I, corresponding to 28 August), two particular M surfaces are identified. The innermost M surface begins near 40 km radius (the edge of the inner Doppler-radar data region on this day) and slopes upwards to 10 km height and outwards to 100 km radius. In subsequent panels, this surface becomes more upright and moves inwards to near 25 km radius, where the eyewall has developed and the Doppler radar data are adequate to apply the analysis methodology. At outer radii, a qualitatively similar evolution is observed. The second M surface highlighted in the top-left panel of Figure 5 is seen initially near 140 km radius and during the next 48 h hours

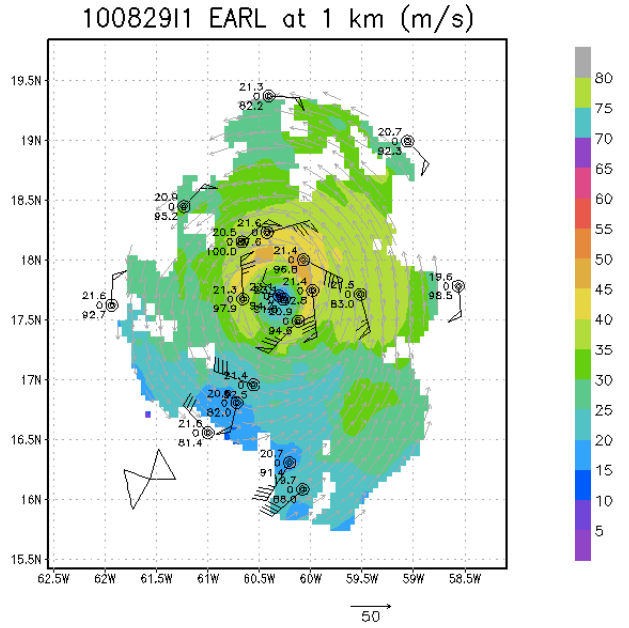

Figure 6. Doppler-radar derived wind vectors for hurricane Earl on 29 Aug (period 1) at a height of 1 km. The wind barbs from the dropwindsonde soundings at this level are superimposed. Doppler-derived wind speeds are color coded according to the scale on the right of the figure.

extends vertically and moves inwards to approximately 70 km radius on 30 August (panel 0830H). A similar behaviour is found with the third M surface that enters the domain by 30 August near 125 km (panel 0830I). Over the next three days, this third M surface moves inwards approximately 20 km and extends vertically. In summary, the M surfaces are found to be moving inwards during the period of observations. Although there is some tendency of the M surfaces to bow inwards near 2 km altitude outside of the RMW, we are cautious of attributing much significance to this feature on account of the difficulty of extracting Doppler data at low altitudes.

5. Dropwindsonde analysis and results

5.1. *Spin up in the boundary layer*

To assess the boundary-layer spin-up mechanism, we study next the boundary layer structure using the dropsonde data with a focus on below 2 km altitude in the vicinity of the high wind region of the vortex. Figure 6 shows an example of the dropwindsonde wind data at a level of 1 km obtained during period 1, an interval sampling the rapid intensification period (cf. Figure 1b). The Doppler-radar derived wind field (described in the foregoing section) are shown at the same level and time period. The figure broadly supports the assumption that the horizontal wind field in the high-wind region possesses a fair degree of symmetry during this period. Similar figures during the other periods have been constructed (not shown) and together they imply that the composite methodology employed herein should provide a meaningful estimate of the azimuthally-averaged vortex structure.

Figures 7-10 display the individual and composite vertical profiles of storm-relative tangential (V_t) and radial (V_r) wind velocities in the eyewall region for the four periods of interest, respectively. The eyewall region, and the associated RMW, is determined from the radar data as described in the foregoing subsection. In these figures, individual dropsondes within 5 km of the RMW are shown in colour while the thick black line is the arithmetical-mean vertical profile of the dropsondes. The full 10 m vertical resolution of dropsondes is being used here to plot the profiles shown.

Aside from the first set of vertical profiles before rapid intensification has commenced (Figure 7), the averaged profiles indicate that the maximum tangential wind speed occurs persistently deep within the vortex boundary layer as defined by the layer of strong inflow (Zhang *et al.* 2009, 2011, Smith *et al.* 2009). For example, Figure 8 shows that between 18 Z 29 Aug and 6Z 30 Aug, the maximum composite tangential wind occurs at a height of 400 m, where the mean inflow magnitude exceeds 15 m s^{-1}. Similarly, between 18 UTC 1 September and 6 UTC 2 September, the maximum composite tangential wind occurs at 500 m and the mean inflow exceeds 30 m s^{-1}! Between 6 UTC 2 September and 18 UTC 2 September, the composite tangential wind profile shows some weakening in intensity relative to the previous period, but the maximum tangential wind speed occurs at approximately 750 m where the mean inflow magnitude is still quite significant, 25 m s^{-1}. As discussed in prior and recent work (Willoughby 1995, Smith et al. 2009, Bui *et al.* 2009, Montgomery and Smith 2013), this layer of strong inflow is driven primarily the net effective radial pressure gradient brought about by surface friction.

The dropsonde data have the advantage of measuring boundary-layer structure with reasonably high vertical resolution (10 m). For a well-developed storm such as Earl, it is reasonable to assume that the pressure field in the boundary layer is to a first approximation axisymmetric. Then we can estimate the radial profile of pressure at each height by fitting a curve to the pressure observations at each drop location. Using this pressure profile, we may calculate the gradient wind at each analysis height, following the method of Sanger *et al.* (2013), Bell and Montgomery (2008) and Kepert (2006a,b). Gradient wind balance is defined as a balance between the radial pressure gradient force per unit mass and the sum of centrifugal and Coriolis forces:

$$\frac{1}{\rho}\frac{\partial p}{\partial r} = \frac{V_g^2}{r} + fV_g \qquad (1)$$

where V_g is the gradient wind. The gradient wind is obtained by solving the quadratic equation for V_g using the calculated radial pressure gradient as long as the radial pressure gradient remains positive.

Figure 11 and shows the results for the gradient wind calculations for the four periods at the height of the maximum tangential wind speed. The left panels show the observed pressure from individual sondes (blue circles) as a function of radius. Shown also are the best fit of the pressure data (red curve) in a quadratic polynomial form using a least square regression method. The right panels show the observed tangential wind corresponding with each pressure observation. For comparison, the gradient wind is presented as a function of radius also (green curve). The red square in each right panel indicates the averaged value of V_t for the eyewall region. In this region for all periods, the average V_t is significantly higher than the corresponding gradient wind. Specifically, this average wind exceeds the gradient wind by 20% during period 1, 43% during period 2, 60% during period 3, and 32% during period 4. These calculations

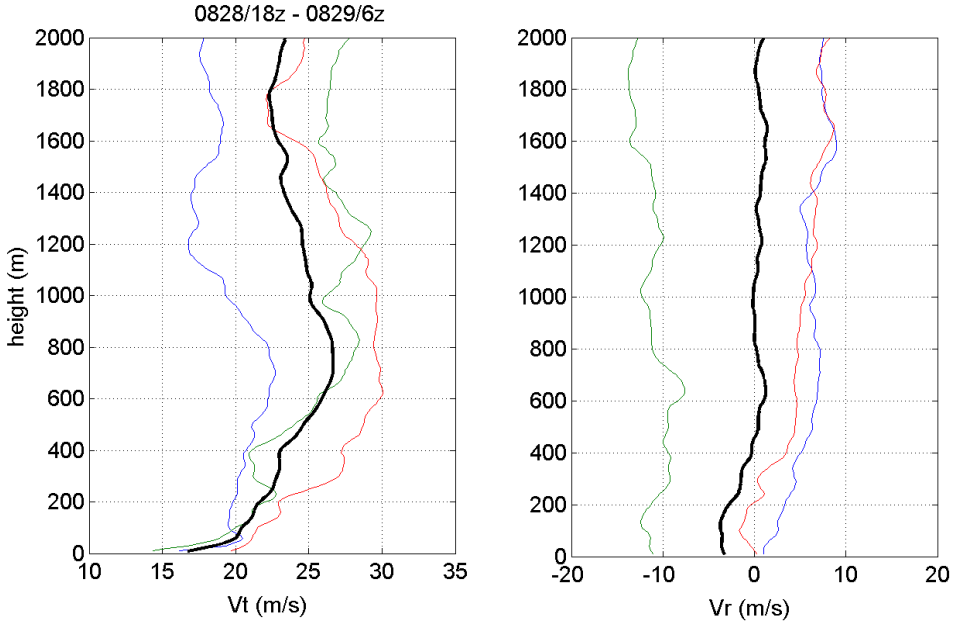

Figure 7. Vertical profiles of storm-relative tangential (V_t) and radial (V_r) wind composites and deviations thereto in the eyewall region of the vortex during the period 1: 0828/18Z - 0829/06Z. The eyewall region is defined as the region within 5 km from the RMW deduced using the Dopper radar data. Curves for the same sounding have the same colour. Dark solid curves represent the arithmetic average of dropsonde data within the eyewall region. Maximum V_t is generally located well within the boundary layer, while the maximum V_r is often very close to the surface. The average height of the maximum tangential wind and maximum inflow during this time is 700 m and 180 m, respectively (see Table 1).

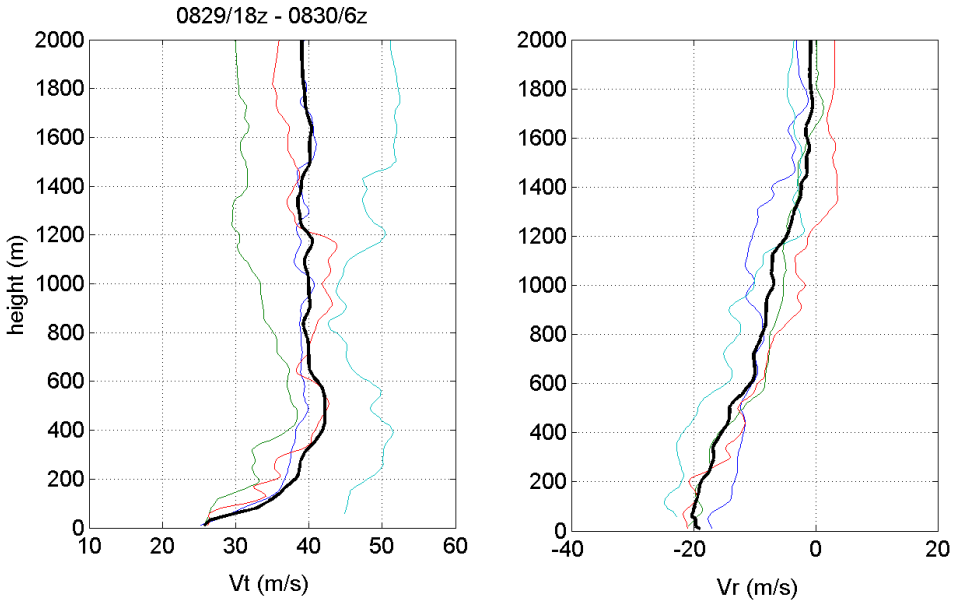

Figure 8. Vertical profiles of storm-relative tangential (V_t) and radial (V_r) wind composites and deviations thereto in the eyewall region of the vortex during the period 2: 0829/18Z - 0830/06Z. The eyewall region is defined as the region within 10 km from the RMW deduced using the Dopper radar data. Curves for the same sounding have the same colour. Dark solid curves represent the arithmetic average of dropsonde data within the eyewall region. Maximum V_t is generally located well within the boundary layer, while the maximum V_r is often very close to the surface. The average height of the maximum tangential wind and maximum inflow during this time is 570 m and 50 m, respectively, while the average height of the inflow layer is 1500 m (see Table 1).

suggest that during both the rapid intensification and quasi-steady periods the boundary layer flow is significantly supergradient at the height of the maximum tangential wind speed. In contrast to the unbalanced state of affairs in the inner-core boundary layer, Figure 11 shows that at outer radii the tangential winds are on average much closer to the gradient wind, albeit somewhat sub-gradient as is to expected where the radial advection of M is considerably weaker. At these radii, the boundary layer is more akin to that of a classical Ekman layer.

During spin up and maturity, the maximum tangential winds occur without exception within the layer of strong boundary layer inflow (< 1 km depth). The tangential winds near the radius of maximum wind in the boundary layer are persistently and significantly supergradient. For brevity, we have shown this feature only at the height of

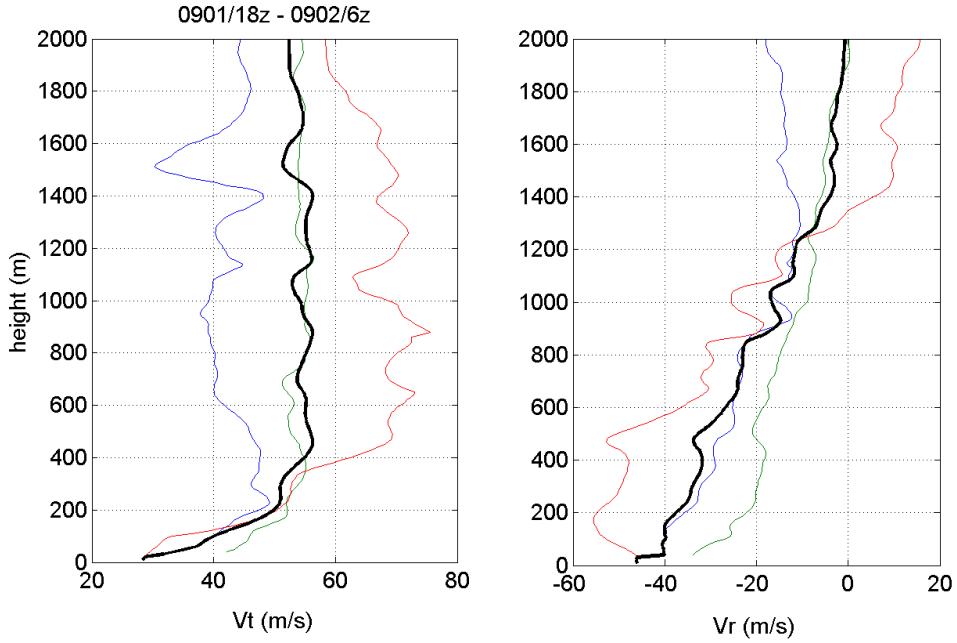

Figure 9. Vertical profiles of storm-relative tangential (V_t) and radial (V_r) wind composites and deviations thereto in the eyewall region of the vortex during the period 3: 0901/18Z - 0902/07Z. The eyewall region is defined as the region within 10 km from the RMW deduced using the Doppler radar data. Curves for the same sounding have the same colour. Dark solid curves represent the arithmetic average of dropsonde data within the eyewall region. Maximum V_t is generally located well within the boundary layer, while the maximum V_r is often very close to the surface. The average height of the maximum tangential wind and maximum inflow during this time is 450 m and 50 m, respectively, while the average height of the inflow layer is 1500 m (see Table I).

maximum tangential wind, but supporting analyses confirm this tendency throughout much of the boundary layer except very near the surface where the tangential winds become subgradient. The average maximum tangential wind speeds beneath the eyewall exceed the gradient wind by between 20% and 60%, with the largest excess occurring during the re-intensification period following the eyewall replacement on 2 September. As an indication of the inaccuracy of the gradient wind for characterizing the structure of the vortex in the boundary layer, the radius of the gradient wind maximum is up to three times the radius of the maximum observed tangential wind speed.

In the foregoing calculations, there is a potential issue regarding the apparent scatter of the tangential wind data relative to the computed gradient wind. To address this concern, we recomputed all of the gradient wind calculations for the boundary layer region using a layer-average of the tangential winds over the layer between 400 m to 1000 m, and computed the gradient wind using the dropsonde pressure field at the mid point of this layer (i.e., 700 m altitude). The results (not shown) corroborate the previous findings. For the case of period 1 (early intensification from the tropical storm stage), the results show that there is still a clear tendency of the inner-core tangential winds to exceed the gradient wind values near the RMW; for one particular sonde inside the RMW the layer-averaged tangential winds exceed the gradient wind by nearly 50%. As the storm intensifies, the difference between the layer-averaged tangential wind and gradient wind increases significantly. These features are to be expected if the boundary layer is exerting a progressively stronger control on the vortex circulation (Montgomery and Smith 2011; Smith *et al.* 2012). In summary, the layer-averaged results support the original calculations and suggest that the boundary layer spin up mechanism, which is responsible for generating the supergradient winds, is active even during the early intensification phase from the tropical storm vortex.

5.2. Testing Carrier et al.'s prediction for the near-surface wind speed

The data presented above offer a unique opportunity to determine the actual near-surface wind in terms of the gradient wind, which is predicted by Emanuel's potential intensity theory for a steady-state hurricane (E86, Emanuel 1995, Bister and Emanuel 1998, Emanuel 2004). The question is: to what extent does Emanuel's potential intensity theory for the gradient wind provide a measure for the total wind speed at the surface? Long ago, Carrier *et al.* (1971), Carrier (1971) and related investigations by Carrier *et al.* (1994, and refs.) predicted that the *total wind speed* in the boundary layer at any height is approximately equal to the gradient wind at the top of the boundary layer. Of course, according to the standard boundary-layer approximation, the gradient wind is approximately uniform throughout the boundary layer. If true, the Carrier prediction would imply that Emanuel's potential intensity theory would be a good approximation to the near-surface wind, which is the preferred measure of intensity used by hurricane forecasters. Restricting attention to the rapid intensification and mature stages of the hurricane, i.e. Figures 8 and 9 and Figures 11(d) and (g), it is evident that the near-surface wind speed at the RMW is approximately 33 m s^{-1} and 56 m s^{-1} compared with gradient wind speeds of 30 m s^{-1} and 36 m s^{-1} , respectively. Under these conditions the surface wind speeds are underestimated by 10% and 55%! Although the maximum gradient wind during these times is marginally larger, 33 m s^{-1} and 50 m s^{-1}, respectively, these maxima

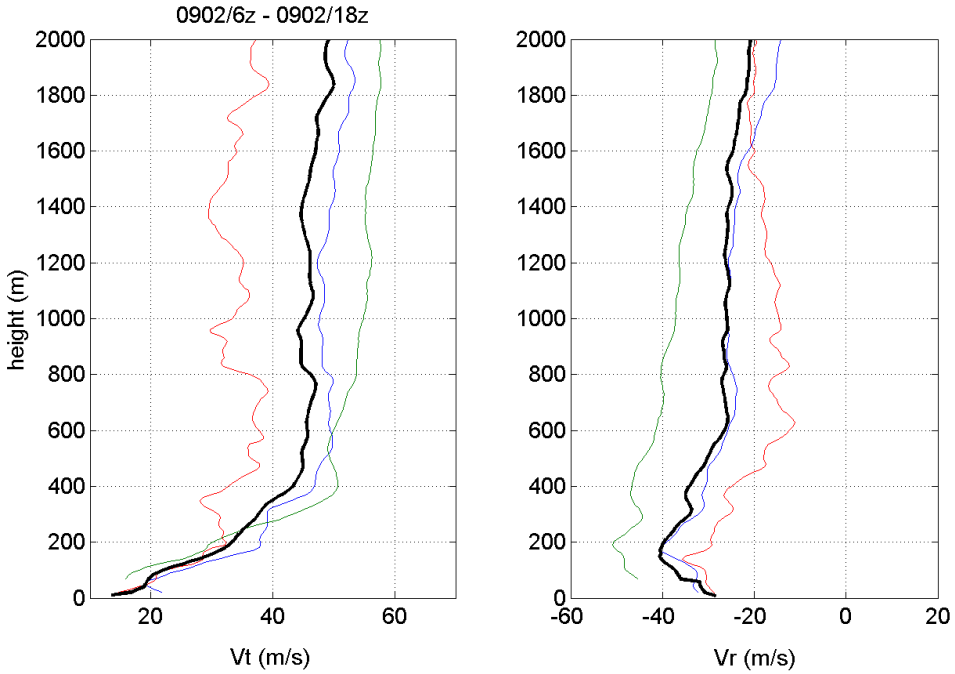

Figure 10. Vertical profiles of storm-relative tangential (V_t) and radial (V_r) wind composites and deviations thereto in the eyewall region of the vortex during the period 4: 0902/06Z - 0902/18Z. The eyewall region is defined as the region within 10 km from the RMW deduced using the Dopper radar data. Curves for the same sounding have the same colour. Dark solid curves represent the arithmetic average of dropsonde data within the eyewall region. Maximum V_t is generally located well within the boundary layer, while the maximum V_r is often very close to the surface. The average height of the maximum tangential wind and maximum inflow during this time is 1800 m and 170 m, respectively, while the average height of the inflow layer is above 2000 m (see Table I).

Period number	Average height of $V_{t_{max}}$ (m)	Average height of inflow layer (m)	Average height of peak inflow (m)	Average surface inflow angle	Percent negative $\partial\|V_r\|/\partial z$
1	700	700	180	12	25%
2	570	1500	50	35	80%
3	540	1800	10	46	50%
4	800	$>$2000	190	57	15%

Table III. Summary of boundary layer parameters for the eyewall region (within 10 km from the RMW) for periods 1, 2, 3 and 4 investigated in this study. These parameters include the average height of the maximum tangential wind speed, the average height of the inflow layer defined nominally (following Zhang *et al.* (2011)) as the height of 10% of the peak inflow, the average height of the peak inflow, the average of the near-surface inflow angle ($\tan^{-1}(-u/v)$), and the percentage of data where $\partial|V_r|/\partial z$ is negative below 200 m, where $|..|$ denotes magnitude and V_r denotes storm-relative radial velocity. The value for the inflow angle is the mean of the lowest 50 m data.

occur at a much larger radius than the maximum tangential wind speed in the observations. Specifically, in the first case, the gradient wind maximum occurs at a radius of 70 km compared with 40 km for the observed tangential wind maximum (Figure 11d), while in the second case the gradient wind maximum occurs at 80 km compared with 25 km (Figure 11f).

5.3. Testing other near-surface characteristics of the boundary layer

The studies by Braun and Tao (2000) and Smith and Thomsen (2010) have elevated awareness of an important problem in the design of deterministic forecast models for hurricane intensity, namely which boundary-layer scheme is most appropriate? They provide estimates also of forecast uncertainty that follow from the uncertainty in not knowing the optimum boundary-layer scheme to use. In an effort to address this issue, Kepert (2012) compared a range of boundary-layer parameterization schemes in the framework of a steady-state boundary-layer model in which the tangential wind speed at the top of the boundary layer is prescribed and assumed to be in gradient wind balance. As a result of his analyses, he argues that boundary-layer schemes that do not reproduce a near-surface logarithmic layer are "badly flawed and should not be used". However, Smith and Montgomery (2013b) present both observational and theoretical evidence that calls into question the existence of a near-surface logarithmic layer in the inner core of a tropical cyclone.

The observational data presented here offer a new opportunity to assess the foregoing issue in the high-wind region of the storm for both the composite boundary layer and individual vertical profiles. From the data shown, the

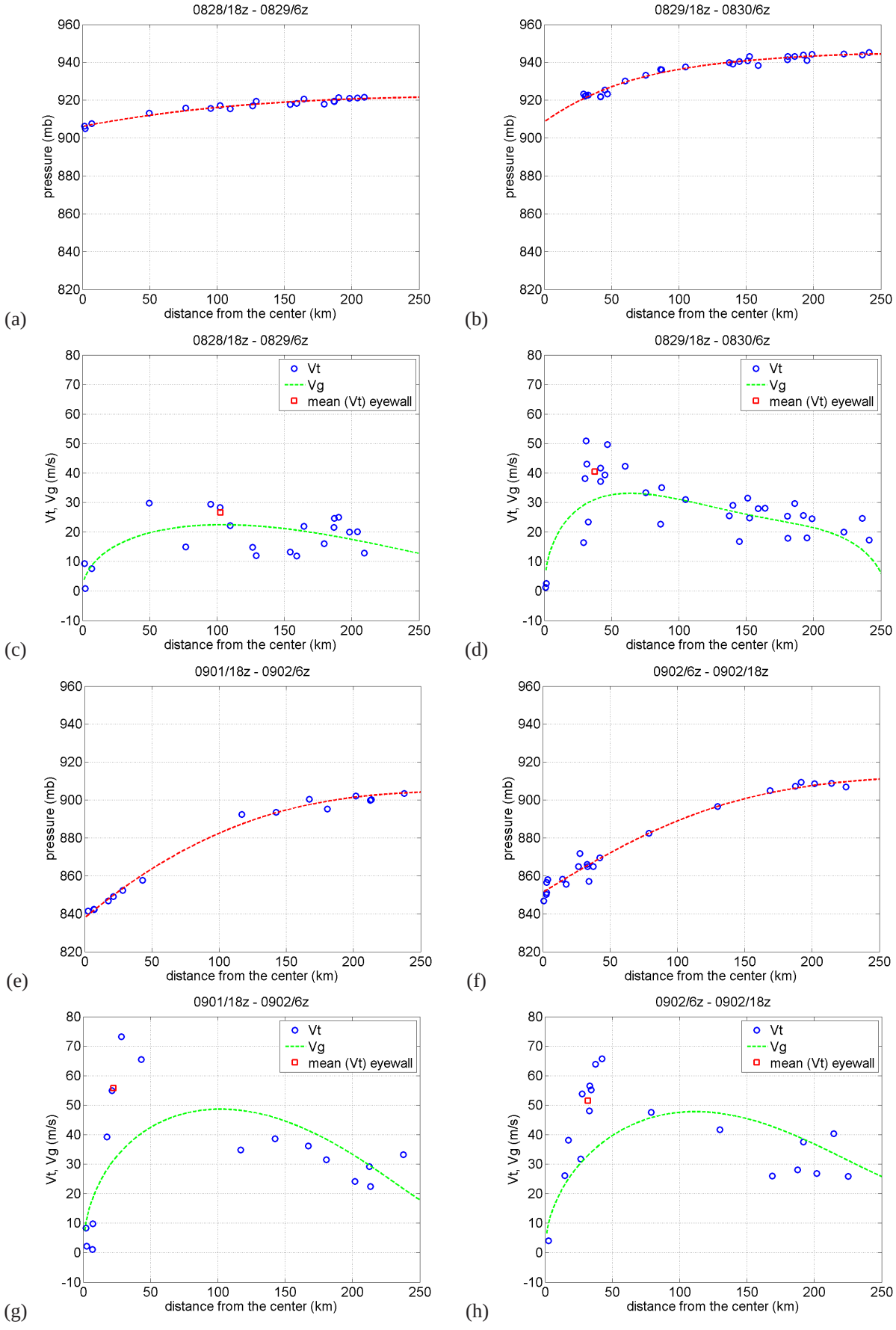

Figure 11. Gradient wind calculation at the height of maximum tangential wind speed (V_t) for periods 1 - 4 (Aug. 28, Aug. 29, Sept. 1 and Sept. 2, see Table I for further details). Calculations are displayed in pairs with dropsonde-observed pressure at the top and dropsonde-observed V_t at the bottom of each plotted pair. For each pair, the top panel shows dropsonde pressure observations (blue) as a function of radius with the fitted curve (red) based on least square regression. Bottom panels show dropsonde observed V_t (blue) and gradient wind V_g (green) as a function of radius. V_g is calculated using the pressure gradient by solving the gradient balance equation. The red square in the tangential velocity plot is the arithmetic average of V_t at the eyewall region within 5 km on either side of the RMW at 2 km altitude inferred from the Doppler radar data.

composite tangential wind component in the boundary layer is a minimum at the surface. While the magnitude of the composite tangential wind generally increases with height near the surface, that of the composite mean radial velocity decreases with height, except in a relatively shallow layer above the sea surface during the intensification and mature stages. Thus, the maximum radial inflow is very close to the sea surface, which is consistent with fluid dynamical considerations for a rapidly rotating vortex adjacent to a frictional boundary (e.g., Bödewadt 1940, also Schlichting 1968, Ch. 11).

The shallow layer of increasing radial inflow is below 50 m during period 1, below 100 m during period 3 and below 200 m during the early weakening stage of period 4. Interestingly, a negative vertical gradient of composite mean radial velocity is evident throughout the boundary layer during period 2. During this period, the maximum mean inflow resides within 50 m from the surface. In those profiles where the radial wind speed increases slightly with height below approximately 100 m, we cannot definitively rule out the existence of a shallow log profile for the composite mean boundary layer structure. Nevertheless, for reasons given by Smith and Montgomery (2013b), we *can* rule out a strict log layer extending two hundred metres in depth as proposed by Powell (2003) for inferring drag coefficients at major hurricane wind speeds. However, for reasons given in Smith and Montgomery (2013b), the subsequent decrease in the magnitude of the radial wind component above this height is not consistent with a traditional log-layer. The data in Table 3 (last column) show that the percentage of eyewall soundings with a negative vertical gradient of the radial wind magnitude is up to 80 % (!), challenging the notion that there is always a shallow log layer in the inner core of a hurricane vortex (cf. Smith and Montgomery 2013b).

The observational data presented offer also an opportunity to examine the surface inflow angle and to compare these with previous observations and the predictions of different boundary layer schemes (Smith and Thomsen 2010). Surface inflow angles derived from recent observational studies of Hurricane Georges (1998), Hurricane Mitch (1998), Hurricane Danielle (1998) and Hurricane Isabel (2003) show maximum inflow angles of 24, 18, 24 and 26, respectively[3]. From their comparison with five different boundary layer schemes, Smith and Thomsen *op. cit.* found a range of inflow angle values between 17 and 35 ^{o} depending on the particular boundary layer scheme. However, from Table I, the average surface inflow angle in the eyewall region for the different observation periods of Earl show surface inflow angles of 12, 35, 46, 57^o, for periods 1,2,3 and 4, respectively. These values are consistent also with the composite analysis of surface inflow angle presented by Zhang and Uhlhorn (2012). In this respect, these observations suggest that the boundary layer schemes studied by Smith and Thomsen are within the range of observed variability.

[3]The first of these angles is based on the right panels of the first and third rows of Figure 9 in Kepert (2006a), the second on panels (b) and (d) of Figure 6 in Kepert (2006b), the third from the second panels of each column of Figure 4 in Schwendike and Kepert (2008) and the fourth on the two right panels of Figure 19 in the same article.

5.4. *Testing gradient wind balance above the boundary layer*

It is widely thought that gradient wind balance holds above the boundary layer (e.g., Willoughby 1990, 1995). The extensive dropsonde data collected offers an opportunity to test this assumption up to the level of the dropsondes using the same methodology of the foregoing subsection. We have carried out these calculations for the height level of 2 km. This altitude is below the altitude of release for all sondes, but still above the strong inflow layer associated with surface friction, so it may be legitimately considered part of the low-level vortex interior. The results are summarized in Figures 12a,c (for period 1), 12b,d (for period 2), 12e,g (for period 3) and 12f,h (for period 4), respectively. In broad terms, there is a clear tendency for the tangential winds near and inside the RMW to exceed the gradient wind even at this altitude. For the period commencing with tropical storm strength winds (period 1), there is again a modest, but clear tendency for the inner-core winds to exceed the gradient wind values near and inside the RMW. For one particular sonde inside the RMW, the tangential winds exceed the gradient wind by nearly 50% at this altitude above the frictional boundary layer. From the other figures, it is evident also that as the storm intensifies, the difference between the gradient and tangential wind increases significantly with storm intensity above the boundary layer. These results differ from those of Willoughby (1990) who concluded using flight-level data that the flow above the frictional boundary layer (above the level corresponding to 850 hPa) is very close (less than 1.5 ms^{-1}, with no bias) to gradient wind balance. These results support the argument summarized in the Introduction that the boundary layer spin up mechanism contributes to the amplification of the interior tangential wind field by lofting air with high tangential momentum from the boundary layer. Echoing our remarks above, these features are to be expected if the boundary layer is exerting a progressively stronger control on the vortex circulation (Montgomery and Smith 2011; Smith *et al.* 2013). In summary, the results suggest that the gradient wind balance approximation above the boundary layer may not be as accurate as has been widely held in the inner-core region of a tropical cyclone during its intensification.

5.5. *Thermodynamic structure in the boundary layer*

As discussed in the Introduction, it is desired to learn more about the thermodynamics of the boundary layer and lower troposphere during the intensification process. In previous work we examined the inner-core and outer-core thermodynamic structure by simply binning the data into two radial groups, the eyewall region and the outer core region (Smith and Montgomery 2013a). We use now the data to construct radial profiles of boundary layer θ_e at both the 100 m and 1500 m levels. The results are shown in Figure 13 for three separate periods. At both levels, the increase of θ_e with decreasing radius is approximately monotonic within 150 km radius. The radial gradient of θ_e is relatively weak during the intensification phase, but becomes quite pronounced during the mature phase of the vortex evolution. At both levels, the difference between θ_e at the axis and 150 km radius increases from about 5 K to 20 K over the observation period.

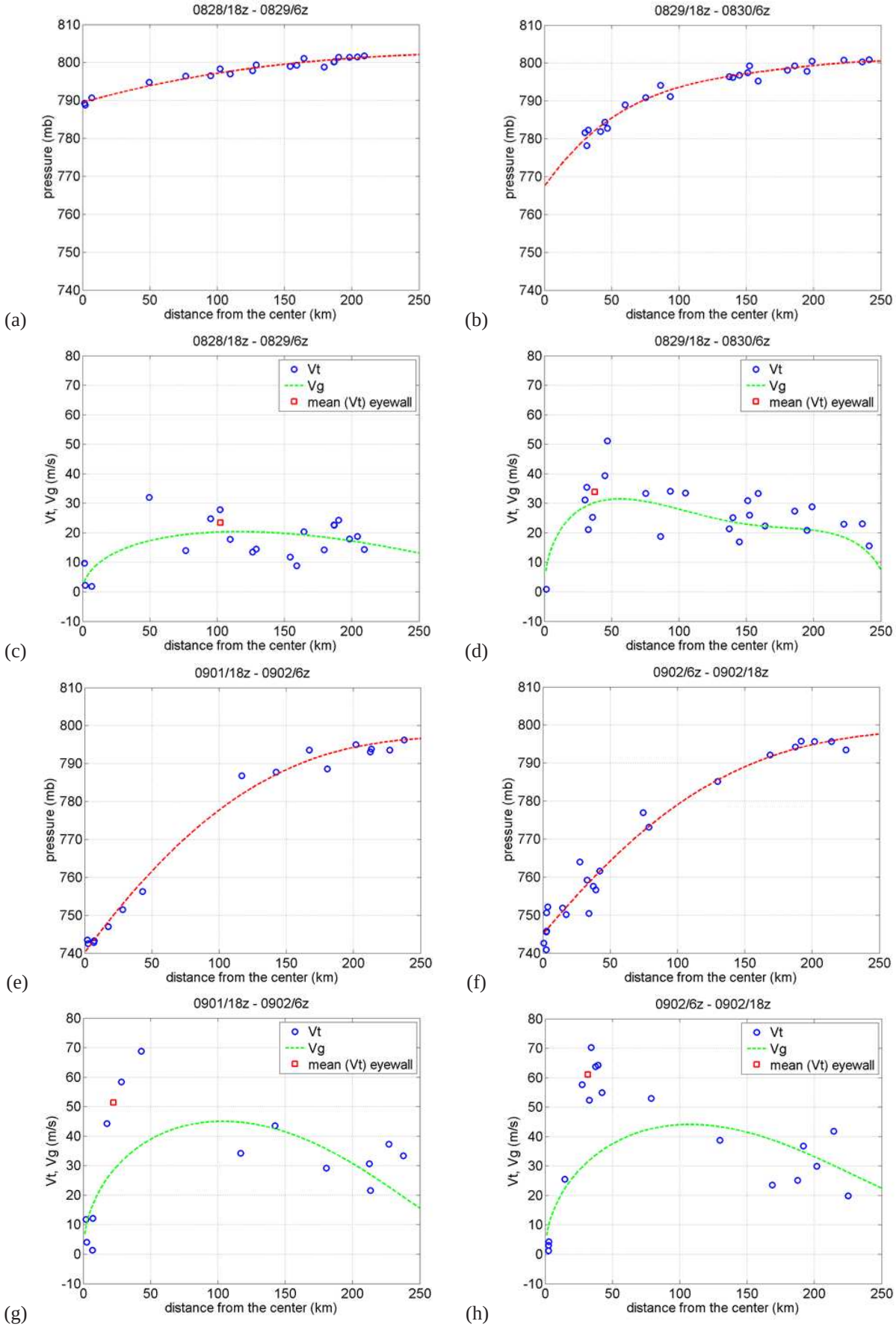

Figure 12. Comparison between gradient wind V_g and tangential velocity V_t at the height of 2 km for observation periods 1 - 4 (see Table I for details). Calculations are displayed in pairs with dropsonde-observed pressure at the top and dropsonde-observed V_t and V_g at the bottom of each plotted pair. For each pair, the top panel shows dropsonde pressure observations (blue) as a function of radius with the fitted curve (red) based on least square regression. Bottom panels show dropsonde observed V_t (blue) and gradient wind V_g (green) as a function of radius. V_g is calculated as in Figure 11. The red square in the tangential velocity plot is the arithmetic average of V_t at the eyewall region within 5 km on either side of the RMW at 2 km altitude inferred from the Doppler radar data.

Montgomery *et al.* (2009) and Montgomery and Smith (2013) noted that a radial increase in near-surface θ_e with decreasing radius is necessary to maintain a degree of convective instability in the inner-core region of a tropical cyclone in the presence of a developing warm core aloft during intensification. Early in the intensification period of Hurricane Earl, the difference in θ_e between the heights 100 m and 1500 m is approximately 10 K beyond 150 km radius and this difference decreases to 8 K as the radius decreases to 50 km near the nascent eyewall. During the rapid intensification and mature period, the difference in θ_e between the heights 100 m and 1500 m is approximately 12 K beyond 150 km radius and this difference decreases to 5 K as one moves inwards to the RMW near the 25 km radius. During the re-intensification period after the eyewall replacement cycle, the difference is somewhat smaller, though the absence of data in this intermediate region cautions us against making quantitative statements.

These observations provide support for a similar finding in high-resolution numerical simulations. In both observations and model, the lack of vertical mixing may be attributable to the large vertical shear in both the tangential and radial winds near the surface. As an illustration, we present in Figure 14 an example from a high-resolution numerical simulation of an intensifying tropical cyclone. The simulation is taken from Smith and Thomsen (2010) using the Blackadar boundary layer scheme (all other boundary layer schemes yield similar results - not shown). Figure 14 shows an azimuthally-averaged radius-height plots of θ_e that looks very similar to the observations shown in Figure 13. Specifically, Figure 14 shows the azimuthally-averaged vertical velocity, radial velocity and corresponding θ_e field. The mean pattern of the vertical velocity field is completely accounted for, yet the radius-height θ_e structure in the lowest levels is remarkably similar Figure 13. These numerical results suggest that the azimuthally-averaged boundary layer θ_e is not well mixed for several hundred kilometres from the centre of the vortex. This finding is contrary to the well-mixed assumption for θ_e invoked in axisymmetric theoretical formulations of the hurricane boundary layer (e.g., Emanuel 1986, 1988, 1989, 1995, 1997, 2003, 2012; Bryan and Rotunno 2009). Here we propose an analogy with the "shear sheltering" concept that has been proffered to explain "anti-mixing" in strongly sheared boundary layer flows (e.g., Hunt and Durbin 1999, Smedman *et al.* 2004) and also in part "eddy transport barriers" (e.g., Dritschel and McIntyre, 2008, and refs.), and hypothesize that the strong vertical shear of the tangential and radial winds in the vortex boundary layer plays an important role in limiting vertical mixing of θ_e in the boundary layer across the broad scale of the hurricane vortex.

In summary, the axisymmetric θ_e structure inferred from the observations at 1.5 km altitude is consistently less than the corresponding near-surface value at all radii, even where the air is ascending into the eyewall. In the inner-most 150 km, the maximum difference is approximately 10 K, while the minimum is about 5 K. These observations suggest that the air going up into the eyewall has significantly lower values of θ_e than those near the surface. This finding is not consistent with the axisymmetric eruption of the boundary layer into the eyewall unless there are non-conservative (eddy) processes acting to modify the entropy of ascending air. As an example, as suggested by D. Raymond (personal communication), the expected high values of θ_e at 1.5 km

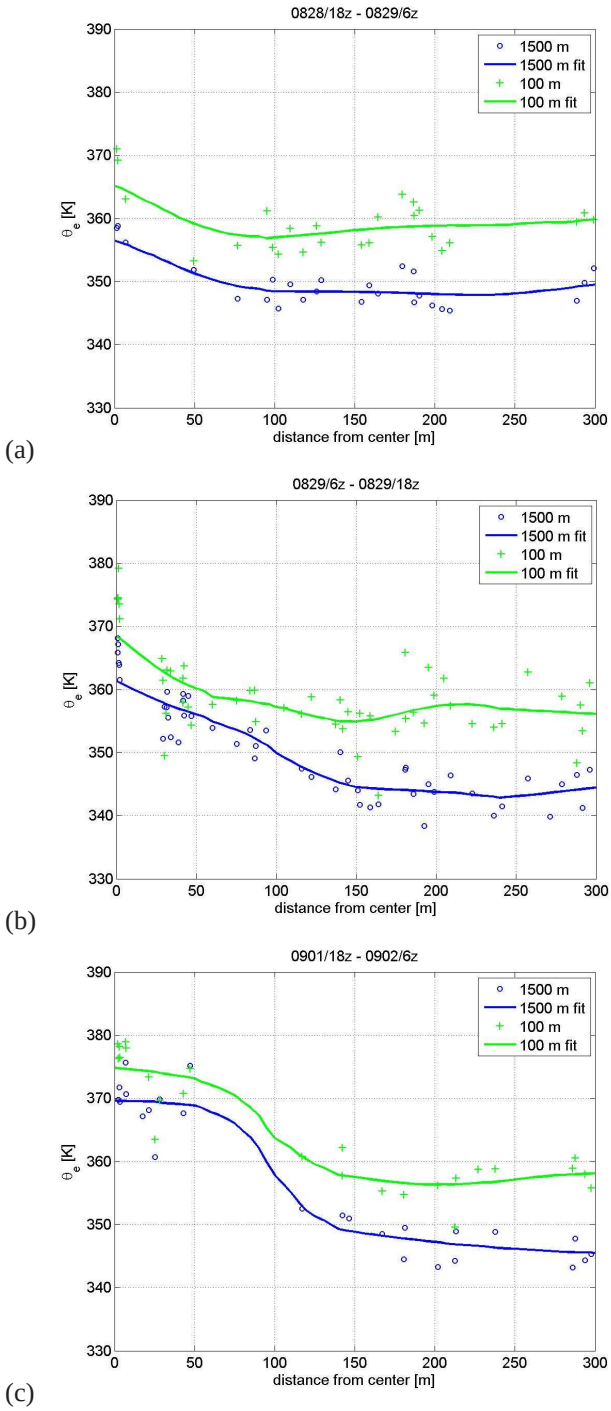

Figure 13. Values of θ_e at a height of 100 m and 1500 m as a function of radius.

may be concentrated in isolated updrafts that were missed by the dropsondes, whereas these θ_e values are more spread out at the surface. If the pilots were deviating around high-reflectivity areas as they penetrated the eyewall, this would almost certainly be the case. These latter considerations implicate an important role of localized updraughts and associated eddy processes in the eyewall region during the intensification of a tropical cyclone (Persing et al. 2013).

The ramification of these thermodynamic findings and interpretations remains a topic for future study, but lies outside the scope of this paper.

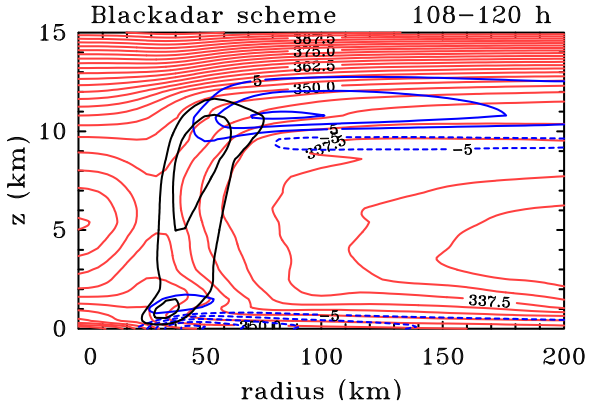

Figure 14. Vertical cross-section of the azimuthally-averaged θ_e-field taken from the mature stage of the idealized numerical simulation described by Smith and Thomsen (2010) using the Blackadar boundary-layer scheme (red contours, contour interval 2.5 K). Superimposed are the isotachs of azimuthally-averaged radial velocity (blue contours, contour interval 5 m s^{-1}) and vertical velocity (black contours, contour interval 0.5 m s^{-1}).

6. Conclusions

We have examined dynamic and thermodynamic aspects of Atlantic Hurricane Earl (2010) during its intensification and mature phases over four days of intensive measurements. The observations are based on a unique data set comprising airborne Doppler-radar and dropwindsondes released from the lower and upper troposphere during the collaborative NASA-GRIP and NOAA-IFEX field studies. These observational resources were supplemented with U.S. Air Force reconnaissance dropwindsonde data. The three and sometimes four aircraft that flew in Earl collected an observational data set that is perhaps the most extensive data set for an intensifying and mature hurricane ever. Here we use these observations to appraise elements of a new model for tropical-cyclone intensification articulated by Montgomery and Smith (2013).

The absolute angular momentum surfaces are shown to move progressively inwards over a deep layer as the storm intensifies. Also, the signature of the strengthening boundary layer inflow is evident by the increase in the upward-outward tilt of the M surfaces in the lower troposphere as these surfaces move inwards. During spin up and maturity, the maximum tangential winds persistently occur within the layer of strong boundary layer inflow (< 1 km depth). The dropsonde composites show that the maximum radial inflow is very close to the sea surface, which is consistent with fluid dynamical considerations for a rapidly rotating vortex adjacent to a frictional boundary.

The tangential winds near the radius of maximum wind in the boundary layer are persistently and significantly supergradient. For brevity, we have shown this only at the height of maximum tangential wind, but supporting analyses over the layer between 400 m to 1000 m confirm this tendency throughout much of the boundary layer except very near the surface where the tangential winds become subgradient. The average maximum tangential winds beneath the eyewall exceed the gradient wind by between 20% and 60%, with the largest excess occurring during the re-intensification period following the eyewall replacement on 2 September. An analysis of the possible departures from gradient wind balance above the boundary layer at 2 km altitude using the same methodology was conducted also. The results suggest that the gradient wind balance approximation in the low-level vortex interior above the boundary layer may not be as accurate as has been widely held in the inner-core region of a tropical cyclone during its intensification. As an indication of the inaccuracy of the gradient wind for characterizing the structure of the vortex, the radius of the gradient wind maximum is up to three times the radius of the maximum observed tangential wind speed. At the radius of the observed tangential wind speed maximum, it is found that the maximum averaged surface wind speed is sometimes significantly underestimated by the gradient wind speed.

The near-surface θ_e and that at a height of 1.5 km increase approximately monotonically with decreasing radius within 150 km of the storm axis. The radial gradient of θ_e is relatively weak during the intensification phase, but becomes pronounced during the mature phase of the vortex evolution. Interestingly, the value of θ_e at 1.5 km altitude is consistently less than the corresponding near-surface value at all radii, even where the air is ascending into the eyewall. Specifically, in the inner-most 150 km, the maximum difference is approximately 10 K, while the minimum is about 5 K. The results suggest that the azimuthally-averaged boundary layer θ_e is not vertically well mixed for several hundred kilometres from the centre of the vortex, contrary to the well-mixed assumption for θ_e invoked in theoretical formulations of the hurricane boundary layer. The observations provide support for a similar finding in high-resolution numerical simulations and support the hypothesis that the lack of vertical mixing of θ_e in nature may be attributable to the large vertical shear in both the tangential and radial winds near the surface.

The axisymmetric vortex structure inferred from the observations suggest that the air going up into the eyewall has significantly lower values of θ_e than those near the surface. This finding is not consistent with the axisymmetric eruption of the boundary layer into the eyewall unless there are non-conservative (eddy) processes acting to modify the entropy of ascending air. These considerations implicate an important role of localized updraughts and associated eddy processes in the eyewall region during the intensification of a tropical cyclone. The ramification of these thermodynamic findings and interpretations remains a topic for future study.

The findings herein complement recent observational work of Sanger *et al.* (2013) and provide further support for the new paradigm of tropical cyclone intensification.

7. Acknowledgements

We acknowledge NASA and Ramesh Kakar for their support of the GRIP experiment. MTM acknowledges the support of NSF AGS-0733380 and NASA grants NNH09AK561, NNG11PK021 and NNG09HG031. JAZ acknowledges the support from NOAA's Hurricane Forecast and Improvement Program (HFIP). We want to thank Sim Aberson and Sylvie Lorsolo for providing the radar composite data for each Earl flight. JAZ is grateful also to Robert Rogers and Paul Reasor for helpful discussions. Finally, we would like to thank Dave Raymond and Jonathan Vigh for their perceptive and constructive reviews.

8. References

Bister M Emanuel KA. 1998: Dissipative heating and hurricane intensity. *Meteor. Atmos. Phys.*, **65,** 233-240.

Bell MM Montgomery MT. 2008: Observed structure, evolution, and potential intensity of Category 5 Hurricane Isabel (2003) from 12 to 14 September. *Mon. Wea. Rev.*, **65**, 2025-2046.

Bödewadt UT 1940: Die Drehströmung über festem Grund. *ZAMM*, **20**, 241-253

Braun SA Tao W-K. 2000: Sensitivity of high-resolution simulations of Hurricane Bob (1991) to planetary boundary layer parameterizations. *Mon. Wea. Rev.*, **128**, 3941-3961.

Bui HH Smith RK Montgomery MT Peng J. 2009: Balanced and unbalanced aspects of tropical-cyclone intensification. *Q. J. R. Meteorol. Soc.*, **135,** 1715-1731.

Bryan GH Rotunno R. 2009: Evaluation of an Analytical Model for the Maximum Intensity of Tropical Cyclones. *J. Atmos. Sci.*, **66**, 3042-3060.

Carrier GF. 1971: Swirling flow boundary layers. *J. Fluid Mech.*, **49**, 133-144.

Carrier GF Hammond AL George OD. 1971: A model of the mature hurricane. *J. Fluid Mech.*, **47**, 145–170.

Carrier GF Fendell F Mitchell J Bronstein M. 1994: Self-sustaining intense vortices. *Physica D*, **77**, 77–96.

Charney JG Eliassen A. 1964: On the growth of the hurricane depression. *J. Atmos. Sci.*, **21**, 68-75.

Dritschel DG McIntyre ME. 2008 Multiple jets as PV staircases: The Phillips effect and the resilience of eddy-transport barriers. *J. Atmos. Sci.*, **65**, 855-874.

Elsberry R Harr P. 2008: Tropical cyclone structure (TCS08) Field experiment scientific basis, observational platforms, and strategy. Asia-Pacific Journal of Atmospheric Sciences, **44**, 1-23.

Emanuel KA. 1986: An air-sea interaction theory for tropical cyclones. Part I: Steady state maintenance. *J. Atmos. Sci.*, **43**, 585-604.

Emanuel KA. 1988: The maximum intensity of hurricanes. *J. Atmos. Sci.*, **45,** 1143-1155.

Emanuel KA. 1989: The finite amplitude nature of tropical cyclogenesis. *J. Atmos. Sci.*, **46**, 3431-3456.

Emanuel KA. 1994: *Atmospheric convection.* Oxford University Press, 580pp.

Emanuel KA. 1995: Sensitivity of tropical cyclones to surface exchange coefficients and a revised steady-state model incorporating eye dynamics. *J. Atmos. Sci.*, **52**, 3969-3976.

Emanuel, KA. 1997: Some aspects of hurricane inner-core dynamics and energetics. *J. Atmos. Sci.*, **54**, 1014-1026.

Emanuel KA. 2003: Tropical Cyclones. *Annu. Rev. Earth Planet. Sci.*, **31**, 75-104.

Emanuel KA. 2004: Tropical Cyclone Energetics and Structure. In *Atmospheric Turbulence and Mesoscale Meteorology*, E. Fedorovich, R. Rotunno and B. Stevens, editors, Cambridge University Press, pp280.

Emanuel KA Rotunno R. 2011: Self-stratification of tropical cyclone outflow. Part I: Implications for storm structure. *J. Atmos. Sci.*, **68**, 2236-2249.

Emanuel KA. 2012: Self-stratification of tropical cyclone outflow. Part II: Implications for storm intensification. *J. Atmos. Sci.*, **69**, in press.

Emanuel KA Neelin JD Bretherton CS. 1994: On large-scale circulations in convecting atmospheres. *Q. J. R. Meteorol. Soc.*, **120**, 1111-1143.

Franklin JL Lord SJ Feuer SE and Marks FD. 1993: The Kinematic Structure of Hurricane Gloria (1985) Determined from Nested Analyses of Dropwindsonde and Doppler Radar Data. *Mon. Wea. Rev.*, **121**, 2433-2451.

Franklin JL Black ML and Valde K. 2003: GPS dropwindsonde wind profiles in hurricanes and their operational implications. *Wea. Forecasting*, **18**, 32-44.

Gamache JF. 1997: Evaluation of a fully three-dimensional variational Doppler analysis technique. Preprints, 28th Conf. on Radar Meteorology, Austin, TX, Amer. Meteor. Soc., 422-423.

Gamache, J. F., cited 2012: Real-time dissemination of hurricane wind fields determined from airborne Doppler radar data. National Hurricane Center. [Available online at http://www.nhc.noaa.gov/jht/2003-2005reports/DOPLRgamache_JHTfinalreport.pdf]

Hawkins HF and Imbembo SM. 1976: The structure of a small, intense hurricane, Inez (1966). *Mon. Wea. Rev.*, **104**, 418-442.

Hock TF and Franklin JL. 1999: The NCAR GPS dropwindsonde. *Bull. Amer. Meteor. Soc.*, **80**, 407-420.

Hunt JCR and Durbin PA. 1999: Perturbed vortical layers and shear sheltering. *Fluid Dyn. Res.*, **24**, 375-404.

Kepert JD. 2006a: Observed boundary-layer wind structure and balance in the hurricane core. Part I. Hurricane Georges. *J. Atmos. Sci.*, **63,** 2169-2193.

Kepert JD. 2006b: Observed boundary-layer wind structure and balance in the hurricane core. Part II. Hurricane Mitch. *J. Atmos. Sci.*, **63,** 2194-2211.

Kepert JD. 2012: Choosing a boundary-layer parameterisation for tropical cyclone modelling. *Mon. Wea. Rev.*, **140**, 1427-1445.

Marks F Houze RA and Gamache JF. 1992: Dual-aircraft investigation of the inner core of Hurricane Norbert. Part I: Kinematic structure. *J. Atmos. Sci.*, 49, 919-942.

Marks FD Black PG Montgomery MT Burpee RW. 2008: Structure of the Eye and Eyewall of Hurricane Hugo (1989). *Mon. Wea. Rev.*, , **136**, 1237-1259.

Montgomery MT Bell MM Aberson SD Black ML. 2006: Hurricane Isabel (2003): New insights into the physics off intense storms. Part I. Mean vortex structure and maximum intensity estimates. *Bull. Amer. Meteor. Soc.*, **87**, 1335-1347.

Montgomery MT Nguyen SV Smith RK Persing J. 2009: Do tropical cyclones intensify by WISHE? *Q. J. R. Meteorol. Soc.*, **135,** 1697-1714.

Montgomery MT Smith RK. 2011. Tropical cyclone formation: Theory and idealized modelling. *In Proceedings of Seventh WMO International Workshop on Tropical Cyclones (IWTC-VII), La Reunion, Nov. 2010.* (WWRP 2011-1) World Meteorological Organization: Geneva, Switzerland.

Montgomery MT Smith RK. 2013: Paradigms for tropical-cyclone intensification. *Aust. Meteor. Ocean. Journl.*, (in press).

Nguyen SV Smith RK Montgomery MT. 2008: Tropical-cyclone intensification and predictability in three dimensions. *Q. J. R. Meteorol. Soc.*, **134**, 563-582.

Ooyama KV. 1964: A dynamical model for the study of tropical cyclone development. *Geophys. Int.*, **4,** 187-198.

Ooyama KV. 1969: Numerical simulation of the life cycle of tropical cyclones. *J. Atmos. Sci.*, **26**, 3-40.

Ooyama KV. 1982: Conceptual evolution of the theory and modeling of the tropical cyclone. *J. Meteor. Soc. Japan*, **60,** 369-380.

Persing J Montgomery MT McWilliams JC and Smith RK. 2013: Asymmetric and axisymmetric tropical cyclone dynamics. *Atmos. Chem. Phys. Discussion*, **13**, 1-116.

Powell MD Vickery PJ and Reinhold TA 2003: Reduced drag coefficient for high wind speeds in tropical cyclones. *Nature*, **422**, 279-283.

Reasor, PD, M. Eastin, and J. F. Gamache, 2009: Rapidly intensifying Hurricane Guillermo (1997). Part I: Low-wavenumber structure and evolution. *Mon. Wea. Rev.*, ,**137**, 603-631.

Reasor PD and M. D. Eastin, 2012: Rapidly intensifying Hurricane Guillermo (1997). Part II: Resilience in shear. *Mon. Wea. Rev.*, **140**, 425-444.

Reasor PD Rogers D and Lorsolo S. 2013: Environmental flow impacts on tropical cyclone structure diagnosed from airborne Doppler radar compoisites. *Mon. Wea. Rev.*, in review.

Sanger N. 2011: An Observational Study of Tropical Cyclone Spinup in Supertyphoon Jangmi and Hurricane Georges. Ph.D. Dissertation. U.S. Naval Postgraduate School. Monterey, California, 120 pp.

Sanger NT, Montgomery MT, Smith RK, Bell MM. 2012: An observational study of tropical-cyclone spin-up in Supertyphoon Jangmi (2008) from 24 - 27 September. *Mon. Wea. Rev.*, in press.

Schlichting, H. 1968: *Boundary-Layer Theory*. 6th ed. McGraw-Hill, 748 pp.

Schwendike J Kepert JD. 2008: The boundary layer winds in Hurricane Danielle 1998 and Hurricane Isabel 2003. *Mon. Wea. Rev.*, **136**, 3168-3192.

Shapiro LJ Montgomery MT. 1993: A three-dimensional balance theory for rapidly-rotating vortices. *J. Atmos. Sci.*, **50**, 3322-3335.

Smedman A-S Hogstrom U Hunt JCR. 2004: Effects of shear sheltering in a stable atmospheric boundary layer with strong shear. *Q. J. R. Meteorol. Soc.*, **130**, 31 - 50.

Smith RK Montgomery MT and Vogl S. 2008: A critique of Emanuel's hurricane model and potential intensity theory. *Q. J. R. Meteorol. Soc.*, **134**, 551-561.

Smith RK Montgomery MT Nguyen SV. 2009: Tropical-cyclone spin up revisited. *Q. J. R. Meteorol. Soc.*, **135,** 1321-1335.

Smith RK Montgomery MT. 2010: Hurricane boundary-layer theory. *Q. J. R. Meteorol. Soc.*, **136**, 1665-1670.

Smith RK Thomsen GL. 2010: Dependence of tropical-cyclone intensification on the boundary-layer representation in a numerical model. *Q. J. R. Meteorol. Soc.*, **136**, 1671-1685.

Smith RK Montgomery MT. 2013a: How important is the isothermal expansion effect in elevating equivalent potential temperature in the hurricane inner core? *Q. J. R. Meteorol. Soc.*, **139** 70-74.

Smith RK Montgomery MT. 2013b: On the existence of the logarithmic surface layer in hurricanes. *Q. J. R. Meteorol. Soc.*, (in press).

Willoughby HE. 1988: The dynamics of the tropical cyclone core. *Aust. Met. Mag.*, **36**, 183-191.

Willoughby HE. 1990: Gradient balance in tropical cyclones. *J. Atmos. Sci.*, **47**, 465-489.

Willoughby HE. 1995: Mature structure and evolution. In *Global Perspectives on Tropical Cyclones. pp21-62. WMO/TD-No 693 (Ed. R. L. Elsberry), World Meteorological Organization, Geneva*, 289pp.

Willoughby HE Chelmow M. 1982: Objective determination of hurricane tracks from aircraft observations. *Mon. Wea. Rev.*, **110**,198-1305.

Zhang D-L Liu Y Yau MK. 2001: A multi-scale numerical study of Hurricane Andrew (1992). Part IV: Unbalanced flows. *Mon. Wea. Rev.*, **129**, 92-107.

Zhang JA Drennan WM Black PG and French JR 2009: Turbulence structure of the hurricane boundary layer between the outer rainbands. *J. Atmos. Sci.*, **66**, 2455-2467.

Zhang JA Rogers RF Nolan DS and Marks FD 2011: On the characteristic height scales of the hurricane boundary layer. *Mon. Wea. Rev.*, **139**, 2523-2535.

Zhang JA Uhlhorn EW. 2012: Hurricane sea-surface inflow angle and an observation-based parametric model of the two-dimensional surface wind field. *Mon. Wea. Rev.*, **140**, 3587-3604.